RESEARCH ARTICLE
SOLID EARTH: COMPUTATIONAL GEOPHYSICS

Earth and Planetary Physics
9: 842–852, 2025
doi: 10.26464/epp2025049

Ab initio molecular dynamics investigation of the proton conductivity and dynamics behavior of hydrous ringwoodite under high temperatures and pressure

SiYu Zhou[1†], DaoHong Liu[1†], ChuanYu Zhang[1*], XuBen Wang[2*], and Li Song[3]

[1]College of Physics, Chengdu University of Technology, Chengdu 610059, China;

[2]College of Geophysics, Chengdu University of Technology, Chengdu 610059, China;

[3]College of Physics, Sichuan University, Chengdu 610065, China

Key Points:

- A first-principles approach is used to study the electrical conductivity of hydrous ringwoodite at high temperatures and pressures.
- Conductivity anomalies in the mantle transition zone in the Craton region and the North Pacific are well explained by computational physics methods.

Citation: Zhou, S. Y., Liu, D. H., Zhang, C. Y., Wang, X. B., and Song, L. (2025). *Ab initio* molecular dynamics investigation of the proton conductivity and dynamics behavior of hydrous ringwoodite under high temperatures and pressure. *Earth Planet. Phys.*, *9*(4), 842–852. http://doi.org/10.26464/epp2025049

Abstract: The electrical conductivity of minerals under extreme conditions is governed by their variations in composition and structure. Constitution water, which is present in various polymorphic phases of olivine, can significantly enhance electrical conductivity under mantle pressure–temperature conditions, therefore playing a key role in proton transport. Despite this, the conductive mechanisms in hydrous olivine, particularly in hydrous ringwoodite, and the dynamic behavior of hydrogen at elevated temperatures, remain poorly understood. In this study, we investigated the proton conduction mechanisms in hydrous ringwoodite through first-principles calculations. Several hydrous models were considered, and *ab initio* molecular dynamics (AIMD) simulations were employed to simulate hydrous configurations at high temperatures. Calculations based on density functional perturbation theory (DFPT) and vibrational density of states (VDOS) analyses were conducted to probe the stability of hydrous structures, and investigate the dynamic behavior of internal hydrogen. Our results indicate that hydrogen trapped in Mg^{2+} and Fe^{3+} defects exhibits significantly higher mobility than hydrogen trapped in Si^{4+} defects. At elevated temperatures, we observed the ionization of hydrogen from cationic defects, leading to high and highly anisotropic proton conductivity along the [100] crystallographic direction. This thermal ionization-induced anisotropic conductivity is consistent with experimental observations of olivine single crystals. Finally, the conductivity of the 0.79 wt% hydrous ringwoodite structure was found to range from $10^{-0.3}$ to $10^{0.4}$ S/m, the 1.19 wt% structure ranged from $10^{0.4}$ to $10^{0.9}$ S/m in the transition region, and the 1.62 wt% structure exhibited conductivity ranging from $10^{0.7}$ to $10^{1.2}$ S/m. These results are in excellent agreement with prior experimental data, providing further insight into the proton conduction mechanisms of hydrous olivine under extreme mantle conditions.

Keywords: hydrous ringwoodite; *ab initio* molecular dynamics; transition zone; lattice vibration; proton conductivity

1. Introduction

The formation of deep-seated Earth rock structures is highly sensitive to changes in the chemical composition of minerals and rocks, as well as the presence and distribution of fluids within the geological system (Huang XG et al., 2005; Yang XZ et al., 2011). Magnetotelluric (MT) sounding studies have identified significant electrical conductivity anomalies at various depths within subduction zones (Wannamaker et al., 2009; Worzewski et al., 2011; Evans et al., 2014; McGary et al., 2014). It is well-established that minerals exhibit a significant reduction in electrical conductivity when exposed to temperatures below their respective melting points. Consequently, a widely accepted hypothesis is that these instances of anomalously high electrical conductivity in the Earth's depths may be a result of partial melting in mineral rock formations (Roberts and Tyburczy, 1999). In contrast to the predominant semiconducting and insulating minerals within the Earth's deep interior, a subset of minerals—such as graphite, ilmenite, and magnetite—is characterized by exceptional electrical conductivity. Moreover, mantle rocks are not only capable of ionic

First author: S. Y. Zhou, zhousiyu@stu.cdut.edu.cn
[†] These authors contribute equally
Correspondence to: C. Y. Zhang, zhangchuanyu10@cdut.edu.cn
X. B. Wang, wxb@cdut.edu.cn
Received 20 JAN 2025; Accepted 15 MAR 2025.
First Published online 30 MAY 2025.

and electronic conduction in certain minerals, but may also exhibit proton conduction (Dai LD and Karato, 2014). A comprehensive analysis of both partial melting and recrystallization models was provided by Karato (2019), emphasizing the complexity of partial melting processes and proposing that hydrogen ion-induced enhancement of mineral electrical conductivity at high temperatures could explain certain geophysical observations.

The presence of even trace amounts of constitutional water in high-pressure minerals can significantly alter their physical and chemical properties, thus influencing the dynamic behavior of the mantle. Constitutional water, in particular, plays a crucial role in modifying the rheological behavior of these minerals. For instance, Wang WZ et al. (2021) employed the Quasi-Harmonic Approximation (QHA) to compute the elastic constants of water-bearing ringwoodite, showing that constitutional water softens the elastic constants under mantle transition zone and lower mantle conditions, influencing both compressional and shear wave velocities. Since the 1960s, research on nominally anhydrous minerals (NAMs) has led to the discovery of OH^- and H_2O in several NAMs. Notably, wadsleyite and ringwoodite have been shown to contain up to 3 wt% constitutional water (Kohlstedt et al., 1996; Rossman, 1996). Karato (1990) was the first to propose that constitutional water within upper mantle olivine significantly enhances its electrical conductivity, primarily due to the high mobility of H^+ ions within the olivine lattice. In further studies, Yoshino et al. (2009) replicated upper mantle conditions using a multi-anvil press, measuring the electrical conductivity of both hydrous and anhydrous olivine at 10 GPa and 2000 K, and revealing a substantial effect of water content on olivine conductivity. Despite these advances, significant challenges remain in understanding the mechanisms underlying the incorporation of water and the effect of H^+ adsorption and dissociation on conductivity in different olivine phases (Du Frane and Tyburczy, 2012). For example, observing the movement of particles in olivine under mantle conditions remains challenging, and existing experimental data have yet to provide a robust theoretical framework for explaining anomalous conductivity changes in the upper mantle and transition zone (Yoshino et al., 2008).

Understanding the hydrogen-assisted enhancement of conductivity is thus critical for interpreting the high conductivity anomalies observed in the mantle transition zone (MTZ). This study aims to investigate the microscopic mechanisms of hydrogen-assisted conductivity enhancement in ringwoodite at the atomic scale using first-principles methods. The conceptual framework is inspired by the high mobility of cations in the superionic phase of solid electrolytes (He Y et al., 2021a), which share structural similarities with aqueous ringwoodite and Li_2O, both exhibiting hexagonal crystal structures. These compounds primarily exhibit ionic bonding, which is highly sensitive to temperature and pressure conditions. Under high-temperature and high-pressure conditions, Li_2O transforms into a superionic conductor, similar to the conditions in the Earth's transition zone, where ringwoodite is located. Consequently, we hypothesize that the conduction mechanism in water-bearing NAMs at high temperatures involves the ionization of constitutional water within ringwoodite, driven by elevated temperatures. This process leads to the formation of a quasi-fluidic proton state with extremely high diffusion rates within the lattice. The electrical conductivity associated with protons in this fluidic state can be described by the Nernst-Einstein relationship:

$$\sigma = \frac{fDCq^2}{k_BT}, \tag{1}$$

where σ is the electrical conductivity of corresponding cation, f is an analytical factor approximately equal to unity, D is the diffusion coefficient, C signifies the ions concentration, q is the electric charge of the cation, k_B is the Boltzmann constant, and T is the absolute temperature.

In summary, through theoretical calculations, this study investigates the diffusion properties of hydrous ringwoodite under the pressure–temperature conditions typical of the MTZ, focusing on evaluating its electrical conductivity characteristics.

2. Structural Details of Hydrous Ringwoodite

Ringwoodite, located within the cubic crystal system (space group: Fd-3m) is characterized by its spinel structure, resulting from the structural transformation of olivine under high pressure. Its chemical formula is typically represented as $A_2B_4O_4$. The structural composition of the mineral consists primarily of two alternating types of atomic layers along the [111] direction. One layer contains MgO_6 octahedra and SiO_4 tetrahedra, while the other layer consists solely of MgO_6 octahedra (Kudoh et al., 2000; Li L et al., 2009).

Previous research has claimed that there are various mechanisms that account for the presence of water in hydrous ringwoodite. The preferred mechanism for water doping in hydrous ringwoodite in nature has been demonstrated to be the hydration mechanism of octahedral cationic vacancies by X-ray single-crystal diffraction (Smyth et al., 2003). Furthermore, under defined thermodynamic conditions, constitution water can coexist in a variety of substitutional forms within a single system (Purevjav et al., 2014). In this investigation, we construct and subsequently perform individual molecular dynamics simulations for five distinct hydrous ringwoodite models.

The first water doping mechanism involves the substitution of two H^+ ions for a single Mg^{2+} vacancy to achieve charge equilibrium, an octahedral cation vacancy hydration mechanism (Smyth et al., 2003), and the stability of the structure is in agreement with what has been observed in practice. The second mechanism entails the substitution of one Mg^{2+} ion and two H^+ ions to occupy a Si^{4+} vacancy, leading to an anti-site substitution mechanism $\left[(Mg)''_{Si}(2H)^{**}\right]^{\times}$, whereby cations originally belonging to the cationic site are removed and anions originally belonging to the anionic site occupy the cationic site (Walker et al., 2007; Verma and Karki, 2009). In the third mechanism, a Si^{4+} vacancy is replaced with four H^+ ions, indicated as $(4H)^{\times}_{Si}$ (Umemoto et al., 2011). Besides, when trivalent Fe^{3+} ions are present within the system, a single H^+ ion couples with Fe^{3+} and becomes integrated into the ringwoodite lattice. Therefore, we have conducted calculations for two coupled substitution hydrous models, where Fe^{3+} and H^+ jointly replace the nearest two Mg^{2+} vacancies to form $\left[(Fe)^{*}_{Mg}(H)'_{Mg}\right]^{\times}$, or both jointly substitute a Si^{4+} vacancy for charge

balance, resulting in $\left[(Fe)'_{Si}(H)^{*}\right]^{\chi}$ (Zhao YH et al., 2004; Withers et al., 2011; Blanchard et al., 2017). It is noteworthy that the protonation sites are located near the edges of the O-O octahedra, with OH vectors subparallel to Mg-O (at an angle of 27.0), and at distances of 1.29 Å and 2.06 Å for Mg-H and Si-H, respectively (Ross et al., 2003). This is analogous to the concept that the possible sites lie between the O-O pairs around the vacant octahedral 16c site (octahedral-tetrahedral hybrid layer) and the 16d site (octahedral layer) (Kudoh et al., 2000).

3. Computational Details

A series of hydrous ringwoodite models were constructed by substituting the appropriate atoms in the Mg_2SiO_4 supercells. Detailed information regarding the atomic numbers and water content of these models is provided in Table 1. Firstly, a series of simulations were carried out using the NPT system at a pressure of 20 GPa, varying the simulation temperature, with a simulation step size of 10,000 steps and a step size of 1.0 fs. Subsequently, data was obtained on the volume evolution over time, and an arithmetic average made of the data from the equilibrium stage, to obtain the extracted data at 20 GPa for the different temperatures. Finally, an equilibrium simulation was carried out using the NVT system. Structural optimizations of all configurations and atomic positions were carried out using the Vienna *Ab Initio* Simulation Package (VASP) code (Kresse and Furthmüller, 1996), employing the Projector-Augmented-Wave (PAW) method based on density functional theory (DFT) (Kohn and Sham, 1965; Blöchl, 1994). The exchange-correlation interactions were treated using the generalized gradient approximation (GGA) with the Perdew-Burke-Ernzerhof (PBE) functional (Perdew et al., 1996). A plane wave basis set for wave function expansion was used, with a cutoff energy of 600 eV. The convergence criteria for electronic self-consistent iterations and ionic relaxation steps were set to 10^{-8} eV and 0.01 eV/Å, respectively, to optimize the hydrogen positions at various sites in all models, thereby ensuring the stability of the initial structures. The K-point mesh in reciprocal space was set to $2\pi \times 0.03$ Å^{-1} to guarantee energy convergence. The vibrational properties of hydrous ringwoodite were calculated at 0 K using the density functional perturbation theory (DFPT; Baroni et al., 2001). The dynamical matrix was subsequently processed using the PHONOPY code, employing a $24 \times 24 \times 24$ q-point mesh (Togo et al., 2023).

The diffusion properties of hydrous ringwoodite were investigated using *ab initio* molecular dynamics (AIMD). To balance computational efficiency and accuracy in AIMD simulations, the cutoff energy was reduced to 400 eV, and Brillouin zone integration was restricted to the Γ point. To ensure convergence, the results were cross-checked using a denser K-point mesh and higher cutoff energy (Figure S1). The initial cell volume was adjusted by expanding it by a factor of two along all three orthogonal crystallographic directions, to create the basis for multiple AIMD simulations conducted under the Nose-Hoover thermostat in the canonical (NVT) ensemble. The Birch–Murnaghan equation of state, derived from anhydrous ringwoodite, was used to calculate the volume (Figures S2 and S3). AIMD simulations of hydrous ringwoodite were performed from 1500 K to 2800 K and 20 GPa using the NVT ensemble for at least 30 ps per simulation to ensure system equilibrium.

4. Results

Based on the hydrous ringwoodite models presented in Table 1, AIMD calculations were initially performed on Model 1, Model 2, and Model 3 (M1, M2, and M3) at varying temperatures to investigate their distinct diffusion behaviors. The mean square displacement (MSD) of atoms as a function of time within the systems was used to characterize the extent of migration at finite temperatures. The MSD is mathematically defined as follows:

$$\langle[\boldsymbol{r}(t)]^2\rangle = \frac{1}{N}\sum_{i=1}^{N}\langle[\boldsymbol{r}_i(t+t_0)^2] - [\boldsymbol{r}_i(t_0)]^2\rangle, \tag{2}$$

where $\langle \boldsymbol{r}_i(t)\rangle$ is the reference position of the target atom at time t, while N is the total number of atoms within the system, and $\langle \boldsymbol{r}_i(t_0)\rangle$ signifies the position of reference time. Consequently, it allows the computation of the diffusion coefficient D, which characterizes the ionic diffusion properties within the system, using the provided expression based on the MSD:

$$D = \lim_{t\to\infty}\left[\frac{1}{2dt}\langle[\boldsymbol{r}(t)]^2\rangle\right]. \tag{3}$$

To investigate the diffusion coefficients of bulk materials, the dimensionless constant d, representing the lattice dimension, is consistently set to 3 within the formula. It is noteworthy that the MSD computed by Equation (3) captures the three-dimensional diffusion motion of ions. Furthermore, it can also be tailored to investigate either the two-dimensional ion diffusion within a specific plane, or the one-dimensional ion diffusion in a particular direction.

The results suggest that at lower temperatures (1500 K for M1 and M3, 1800 K for M2), hydrogen exhibits a propensity to predominantly occupy corresponding cationic vacancies (in M1 and M3),

Table 1. The ringwoodite model configurations for *ab initio* molecular dynamics simulations with different water and iron contents.

Models	Composition	Defects	Water Contents	Fe/(Mg+Fe)
Model 1	$Mg_{15}Si_8O_{32}H_2$	$(2H)^{\times}_{Mg}$	1.63 wt%	0%
Model 2	$Mg_{17}Si_7O_{32}H_2$	$\left[(Mg)''_{Si}(2H)^{**}\right]^{\times}$	1.60 wt%	0%
Model 3	$Mg_{16}Si_7O_{32}H_4$	$(4H)^{\times}_{Si}$	3.27 wt%	0%
Model 4	$Mg_{14}Fe^{3+}Si_8O_{32}H$	$\left[(Fe)^{*}_{Mg}(H)'_{Mg}\right]^{\times}$	0.79 wt%	6.67%
Model 5	$Mg_{16}Si_7Fe^{3+}O_{32}H$	$\left[(Fe)'_{Si}(H)^{*}\right]^{\times}$	0.78 wt%	5.88%

significantly limiting its internal lattice diffusion. Additionally, within M2, hydrogen tends to localize within anti-site defects, where it replaces Mg^{2+} in the position of Si^{4+}, indicating a slightly higher hydrogen diffusion transition temperature compared to the M1 configuration. At high temperatures, prolonged thermal excitation prompts hydrogen to gradually vacate the corresponding cationic vacancies, liberating itself from the cationic defects and diffusing into the interstices of the lattice. As depicted in Figure 1, thermal excitation leads to a gradual increase in MSD over time, approximately demonstrating a proportional growth trend. Nevertheless, within the M3-type hydration mechanism, even at the extremely high temperature of 2400 K, both the time-dependent behavior of MSD in Figure 1a and the paths of hydrogen ions in Figures 1f and 1g reveal restricted hydrogen diffusion. This observation suggests that the strong stability of the hydration mechanism involving Si^{4+} vacancy substitution under high pressure is also indicative of a robust interaction between hydrogen and the Si^{4+} vacancy.

To gain a better understanding of the interaction between two atoms in this condensed system, we investigate the radial distribution function (RDF) $g(r)$, which provides information on the probability of locating a target atom at various distances from a reference atom. This analysis contributes to a deeper understanding of the interatomic interactions and the overall structure of the system. The RDF is defined as:

$$g(r) = \frac{\mathrm{d}N}{4\pi r^2 \mathrm{d}r}/(\rho \mathrm{d}V), \tag{4}$$

where dN is the number of atoms of the target type in the shell of thickness dr and distance r, ρ represents the system density, and dV represents the shell volume.

The RDF derived from AIMD simulations of hydrogen-doped structures in M1 is shown in Figure 2. The RDF obtained from the simulations presents different interaction modes among the target atomic pairs at both low and high temperatures. In Figure 2a**,** the RDF variations with distance r between oxygen (as the reference) and hydrogen atoms (as targets) are displayed. Simulations of both low and high temperatures reveal the isolated peaks in the RDF for O-H pairs around 1.02 Å, indicating the distance where hydrogen atoms in the system are most likely to exist in the space around oxygen atoms during the AIMD simulations, where the corresponding interaction type is the oxygen-hydrogen bond.

For the second peak, corresponding to the second coordination layer of oxygen atoms, the interaction observed for the O-H atomic pairs is indicative of the weak interaction of hydrogen bonds within the system (Kühne and Khaliullin, 2014; Kim et al., 2020). However, analysis of the second RDF peak reveals that at the low-temperature conditions, the peak exhibits a tall and narrow shape, contrasting the broader and shorter pattern observed at high-temperatures. The discrepancy observed in the second peak of the RDF at different temperatures can be

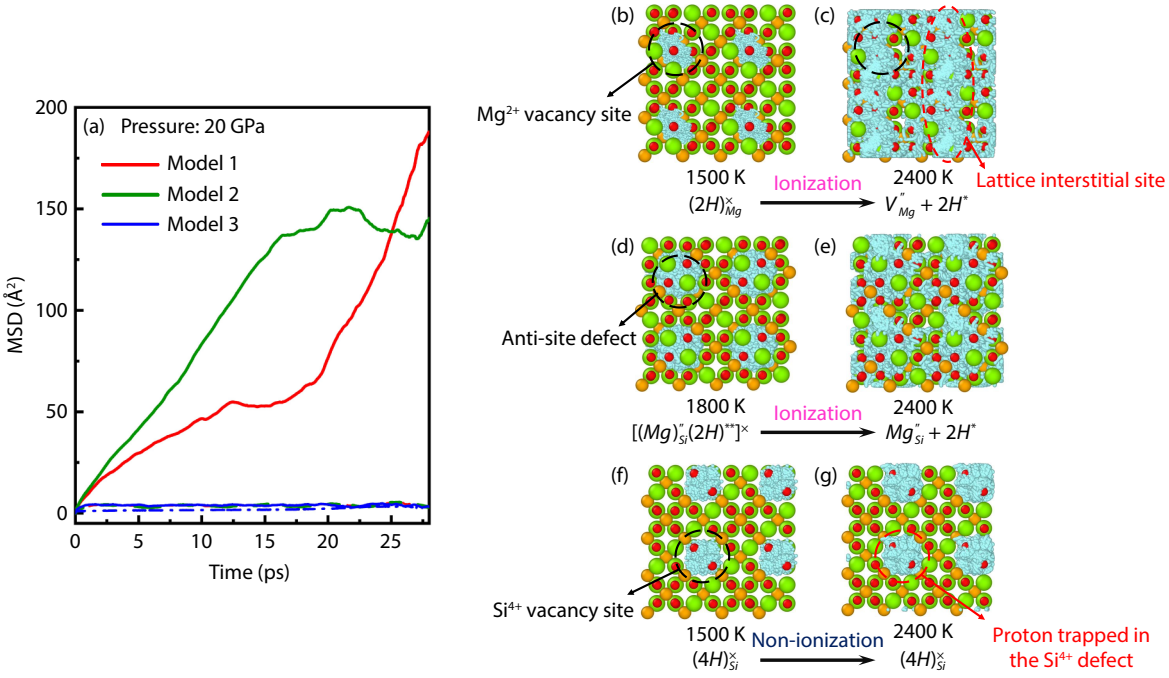

Figure 1. Temporal evolution of the mean square displacement (MSD) of hydrogen ions from AIMD simulations at different temperatures, along with schematic representations of hydrogen migration trajectories within Model 1, Model 2, and Model 3 systems. (a) Illustration of the trend in MSD over time, with dashed lines depicting MSD at lower temperatures (1500 K for Model 1 and Model 3, and 1800 K for Model 2) and solid lines representing MSD at higher temperatures. Over the course of the simulations, Model 1 and Model 2 exhibit a notable increase in MSD over time, while Model 3 displays a considerably stable trend in MSD. Hydrogen migration trajectories within Mg^{2+} vacancies at (b) 1500 K and (c) 2400 K, and within anti-site defects at (d) 1800 K and (e) 2400 K. Additionally, hydrogen motion trajectories confined within Si^{4+} vacancies at (f) 1500 K and (g) 2400 K. The cyan spheres are trajectories of proton migration. Green, orange, and red respectively denote Mg, Si, and O atoms in Mg-pure ringwoodite crystal.

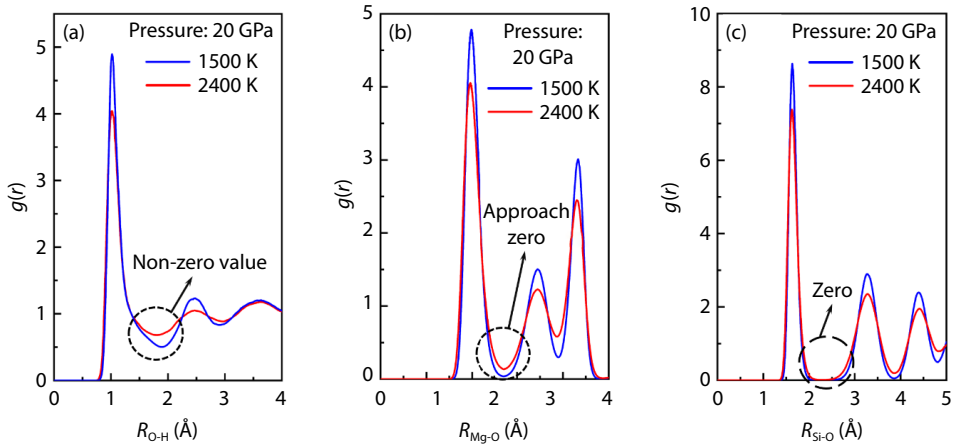

Figure 2. Diagram of the RDFs $g(r)$ for (a) O-H, (b) Mg-O, and (c) Si-O in Model 1 at different temperatures. In particular, the O-H atomic pairs display a non-zero quantity between the first and second coordination peaks, the Mg-O atomic pairs exhibit nearly zero values between the first and second coordination peaks, and between the first and second coordination peaks for Si-O atomic pairs zero value.

attributed to the milder lattice vibrations at lower temperatures, which favor the formation of hydrogen bonds. Conversely, heightened lattice vibrations at high temperatures render atomic interaction severely unstable, resulting in a substantial weakening and potential breakdown of weak bonds like hydrogen bonds. Consequently, increasing temperatures lead to a further reduction in the effects of hydrogen-oxygen and weak hydrogen bonds, evidence of which were observed in the diminishment of the first two values of the RDF peaks and an intensification in proton diffusion. Additionally, a non-zero RDF density exists between the first and second peaks of O-H pairs, with a larger non-zero value at high-temperatures than at low-temperature, suggesting potential breakage and recombination reactions of hydrogen-oxygen bonds during AIMD simulations. At low-temperatures, the lowest non-zero density signifies the localized diffusion behavior of protons within Mg^{2+} vacancies, as represented in Figure 1b, while the highest value at high-temperatures corresponds to proton diffusion in a liquid-like state, diffusing within the interstitial crystal lattice as depicted in Figure 1c.

The RDF profiles for Mg-O and Si-O atomic pairs shown in Figures 2b and 2c exhibit prominent, towering peaks at both high and low temperatures, indicating the strong stability of Mg-O and Si-O bonds under high temperature conditions. Notably, the non-zero density between the first and second peaks in the RDF for Mg-O pairs at 1500 K and 2400 K suggests Mg-O chemical bond breakage and reformation during the AIMD simulation. Nevertheless, these tiny fluctuations do not appear to support the phenomenon of Mg diffusion within the crystal (Figure S4).

In addition, the DFPT method was adopted by Yu YG and Wentzcovitch (2006) to calculate the vibrational properties of anhydrous ringwoodite at high pressures. Here we also used the M1 structure as the initial configuration, deriving the kinetic matrix from vibrational frequencies computed using the DFPT method (Baroni et al. 2001), and post-processing the force constants and phonon frequencies extracted from the kinetic matrix eigenvalues using the PHONOPY code (Togo et al., 2023), to obtain the phonon density of states (PDOS) and dispersion curves reflecting the structural stability of hydrous ringwoodite on the kinetic scale. The vibrational density of states (VDOS) of hydrous ringwoodite with a water content of 1.63 wt% is compared at different temperatures to estimate the effect of constitution water on the vibrational modes of ringwoodite.

At finite temperatures, the VDOS of the system particles can be extracted from the Fourier transform of the velocity autocorrelation function (VACF) of the corresponding particles, denoted as:

$$g(\omega) = \int_{-\infty}^{\infty} \frac{\left\langle \sum_i \boldsymbol{v}(t_0) \cdot \boldsymbol{v}_i(t_0 + t) \right\rangle}{\left\langle \sum_i \boldsymbol{v}(t_0) \cdot \boldsymbol{v}_i(t_0) \right\rangle} \mathrm{e}^{-2\pi i \omega t} \mathrm{d}t, \tag{5}$$

where $\boldsymbol{v}_i(t_0)$ is the particle velocity vector at reference time, and $\boldsymbol{v}_i(t)$ is the particle velocity vector at correlation time, $\langle \cdots \rangle$ denotes the desired value, $g(\omega)$ is the vibrational state density, ω is the frequency, and i denotes the number of particles.

The normalized PDOS and VDOS are depicted in Figure 3. When temperature increases, as illustrated in Figure 3a, the high-frequency vibration peak of hydrogen gradually increases from about 1000 cm^{-1} to about 1250 cm^{-1}, while the low-frequency vibrational peak decreases rapidly. At 1500 K, hydrogen is confined within the sublattice and cannot diffuse into the interstitial space, and a high probability density distribution is observed in the high-frequency channel. At 2400 K, as shown in the subplot of Figure 3a, hydrogen exhibits a non-zero probability density within the zero-frequency channel, which suggests that hydrogen undergoes thermal dissociation and migration in the system, and this transition is further manifested by the shift of hydrogen from a vibrational mode mediated by chemical bonding to the dominant mode characterized by proton translation within the system. However, for both Mg and Si VDOS (shown in Figure 3b and 3c, respectively) the diffusion coefficients in the zero-frequency channel are zero, representing the fact that both elements are fixed in their sublattices at both low and high temperatures. It is worth mentioning that the similarity of both the VDOS and PDOS of magnesium and silicon at high temperatures is due to the fact that both act as backbone components of the ringwoodite, maintaining the stability of the whole crystal, and are not involved in conduction, whereas H is mainly involved in conduction at high

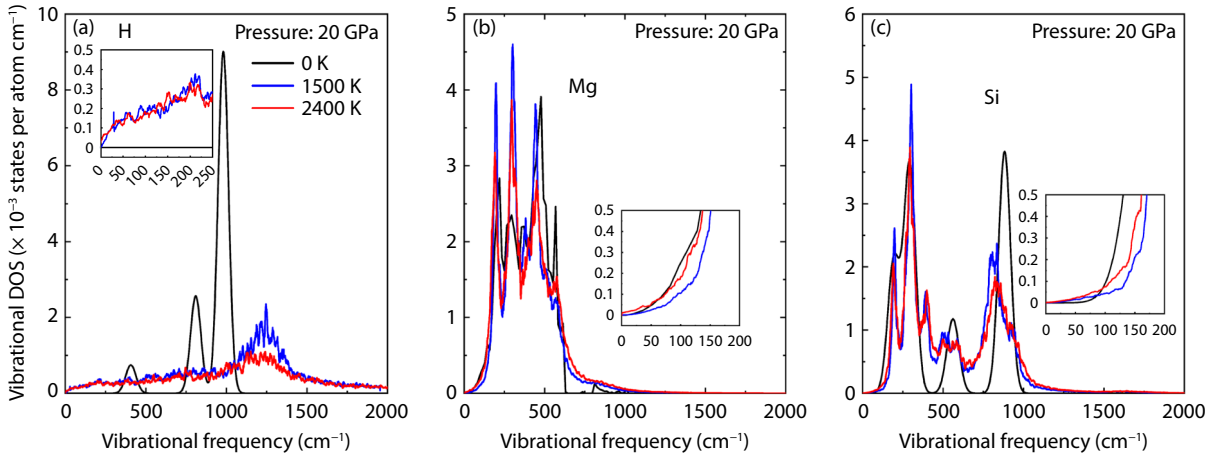

Figure 3. Schematic of the normalized VDOS for the M1 configuration of hydrous ringwoodite. The profile formed by the black curves depicts the PDOS for (a) H, (b) Mg, and (c) Si obtained from static phonon calculations at 0 K. The blue and red curves correspond to the VDOS derived from the Fourier transform of the VACF at 1500 K and 2400 K, respectively. The low-frequency region is locally enlarged in subgraphs, and the zero/non-zero VDOS at zero frequency channel shows the fixed/diffusive behavior of the particles at different temperatures, respectively.

temperatures instead of maintaining the ringwoodite structure. Comparing temperatures of 2400 K to 1500 K, in the case of the 2400 K temperature the protons involved in the conduction states are more gentle, and the number of states in which protons are involved in the conduction states is higher. At the same time, at 0 K, H is obviously not involved in conduction, but as a component of the structure, suggesting that H is dominated by chemical bonding vibration at low temperatures, while the vibrational mode of H is dominated by translational motion at high temperatures.

In evaluating the hydrous models M4 and M5 featuring the trivalent state of iron ions, the AIMD method was employed to explore the thermal dissociation of hydrogen and resulting proton thermal diffusion effects within Fe-bearing hydrous ringwoodite. As depicted in Figure 4, at low-temperature, both water incorporation

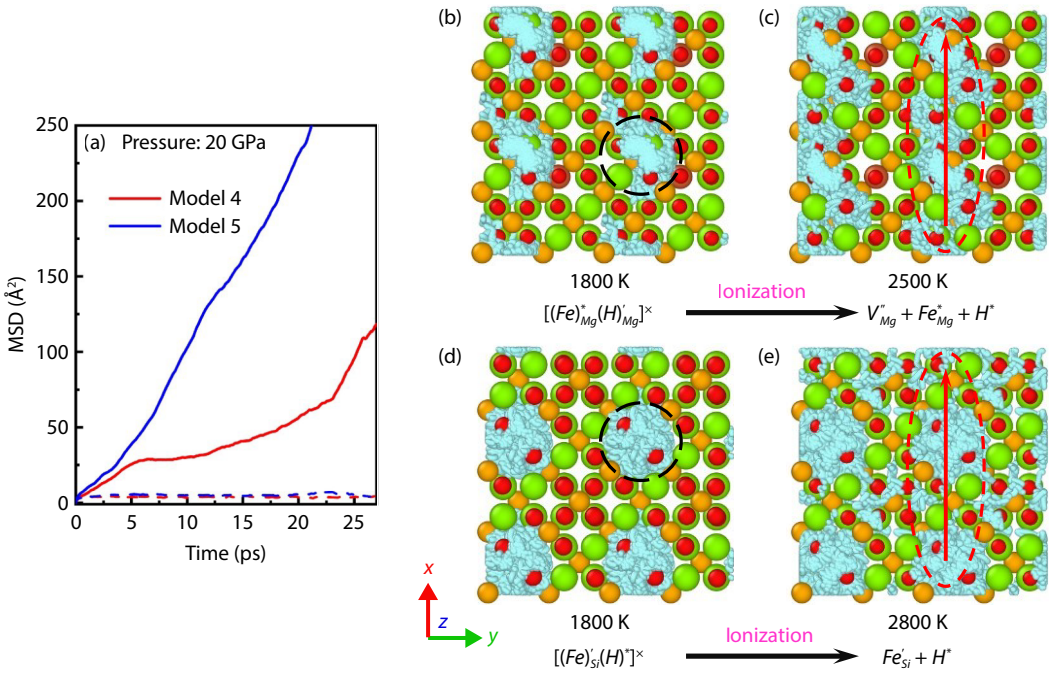

Figure 4. Diagram of the MSD for hydrogen ions and proton migration trajectories of Model 4 and Model 5 (M4 and M5) at different temperatures, obtained from the AIMD. The trend of MSD over time, where dashed lines at low-temperature conditions and solid lines at high-temperature conditions (2500 K for M4 and 2800 K for M5). The trajectories of protons of Fe^{3+} replacing Mg^{2+} vacancies simulated at (b) 1800 K and (c) 2500 K, respectively, while the trajectories of protons of Fe^{3+} replacing Si^{4+} vacancies simulated at (d) 1800 K and (e) 2800 K, respectively. Red arrows signify the primary migration paths of hydrogen along the [100] crystal orientation in M4 and M5, and these trajectories are represented by cyan spheres. Green, orange, red, and dark brown correspond to Mg, Si, O, and Fe atoms in the ringwoodite crystal, respectively.

configurations of M4 and M5 exhibit distinctive low diffusion rates, which are characterized as the localized hydrogen entrapment in the corresponding defects. Conversely, at high-temperatures (2500 K for M4, 2800 K for M5), hydrogen becomes thermally dissociated, escaping the corresponding defects and diffusing into the interstices of the lattice, resulting in significant proton mobility. In addition, the directed protons' motion trajectories are observed in Figure 4c and 4e, indicating a predominant migration along the [100] crystal orientation.

To further investigate the anisotropic migration phenomenon observed in the proton trajectories, the mobility of protons along the three mutually orthogonal directions of [100], [010], and [001] under high-temperature conditions was calculated by using one-dimensional MSD. As shown in Figure 5, the MSD values along the [100] crystallographic direction are significantly larger than those along the other crystallographic directions, which confirms the anisotropic migratory behavior of thermally dissociated protons in Fe-containing hydrated magnesite under high-temperature conditions. This reconfirms the significant effect of Fe^{3+} doping on the proton migration behavior.

5. Discussion

5.1 Behavioral Dynamics of Hydrous Configuration

The results presented in Section 4 comprise a detailed exposition of the dynamic behaviors of hydrous ringwoodite under high-temperature conditions, providing a more intuitive understanding of the phenomena observed in previous high-temperature, high-pressure experiments. In the majority of configurations, hydrogen trapped in cation defects can be ionized at high temperatures. Subsequently, ionized protons can diffuse into lattice interstices, displaying enhanced proton mobility that augments proton conductivity.

In exploring the impact of water on the lattice dynamics of ringwoodite, we then select the M1 structure as the initial configuration to calculate the RDF and VDOS of the water-bearing system. The RDF results reveal instances of breakage and reformation in the Mg-O bond within the simulated temperature range, while the probability density of the Si-O pairs between the first two peaks of RDF shows that the Si-O bond remains stable at high-temperature. Previously, Ye Y et al. (2012) conducted high-temperature, high-pressure experiments on ringwoodite with an average water content of 2.5 wt%, observing in thermal expansion data that MgO_6 octahedra exhibit a more pronounced distortion at high temperatures than SiO_4 tetrahedra. The SiO_4 tetrahedra exhibit lower compressibility in space compared to MgO_6 octahedra, which indicates that Si-O bonds are stronger than Mg-O bonds under the corresponding conditions. This observation aligns with AIMD simulations of the M1 configuration (water content of 1.63 wt%), where the strength of Mg-O bonds is weaker than that of Si-O bonds. In addition, Shimojuku et al. (2009) and Chakraborty (2010) also investigated and summarized the bulk diffusion coefficients of the anhydrous ringwoodite, respectively, showing a diffusion rate of Si that is four orders of magnitude smaller than that of Mg, establishing Si as the predominant rate-controlling species in lattice deformation at the MTZ region.

On the other hand, as shown in Figure 2a, the average hydroxide bond length in hydrous ringwoodite is around 1.0 Å , which is similar to the hydroxide bond length of 1.025 Å calculated by Wang WZ and Wu ZQ (2022). This difference arises due to the ability of hydrogen in the system to migrate within cation vacancies or lattice interstices at finite temperatures, weakening the interactions of hydrogen bonds, which manifests as a decrease in the RDF peak. The high mobility of ionized hydrogen at elevated temperatures leads to more frequent collisions and dissociation of hydrogen in the lattice that in turn promotes more efficient energy transfer, contributing to the observed trend of increasing thermal conductivity in hydrous ringwoodite with rising temperature (Marzotto et al., 2020).

In parallel with the conductivity mechanisms of solid-state electrolytes, the motion of highly mobile protons in hydrous ringwoodite at high temperatures resembles the superionic state

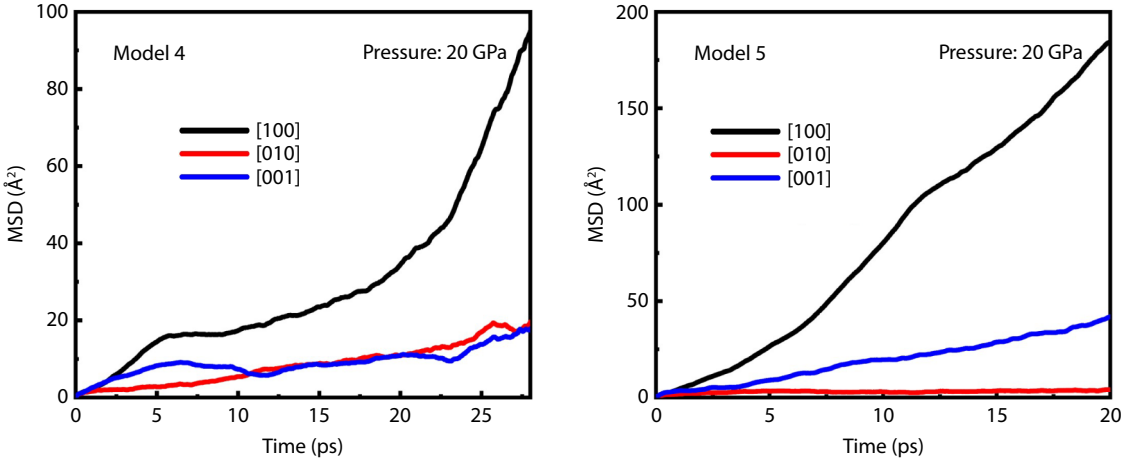

Figure 5. One-dimensional MSD of protons along the [100], [010] and [001] directions. The left side is the MSD of M4 along the respective orthorhombic crystal orientations at 2500 K, and the right side is the MSD of M5 at 2800 K along the respective orthorhombic crystal orientations. The increase of time-dependent MSD along the [100] direction is significantly larger than in other directions, which fully indicates the anisotropic migration behavior of protons.

observed in Li^+ in lithium compounds (He Y et al., 2021b; Krenzer et al., 2022). Correspondingly, Liu C et al. (2019) observed a high mobility phenomenon of superionic hydrogen and helium at high temperatures based on the AIMD simulations of He-H_2O compounds.

5.2 Proton Diffusion Coefficient and Activation Enthalpy

In order to elucidate the dependency of proton diffusion rates on temperature, we conducted extensive *ab initio* molecular dynamics (AIMD) simulations for M1–M5 at various temperatures, subsequently calculating the corresponding proton diffusion coefficients, as shown in Figure 6. The diffusion coefficient, denoted as D, demonstrates a robust correlation with temperature, a phenomenon conventionally explicated by the Arrhenius equation:

$$D = D_0 \exp\left(-\frac{\Delta H}{k_B T}\right), \tag{6}$$

where D_0 represents the pre-exponential factor, ΔH is the activation energy, k_B is the Boltzmann constant, and T signifies the absolute temperature. The activation enthalpies for proton diffusion in various configurations were computed using Equation (6). For the water incorporation configurations M1 and M2, the activation enthalpies are determined to be 130.27 kJ/mol and 82.71 kJ/mol, respectively. Meanwhile, the hydrous configurations of M4 and M5 demonstrate similar activation enthalpies, approximately 186.42 kJ/mol, which are significantly higher than the hydrogen diffusion activation enthalpies calculated in previous high-temperature and high-pressure experiments on water-related conductivity of ringwoodite (101 kJ/mol; Sun W et al., 2015) under lower water content conditions.

The activation enthalpy of hydrogen diffusion in hydrous ringwoodite configurations, where Fe^{3+} replaces cations, exhibits significant disparities compared to previous experiments. Our conjecture is that the Fe, as a transition metal with correlated electronic effects arising from its 3d orbitals, results in a strong electron–electron (el-el) interaction within the system (Alexandrov et al., 2013). The el-el interaction is larger than the kinetic energy of the atoms in the system, making the Coulomb repulsion resulting from their interaction non-negligible. Moreover, the calculated M4 and M5 configurations reveal a pronounced anisotropic diffusion of hydrogen at high temperatures, with the [100] direction exhibiting the most distinct diffusion behavior. On the other hand, a comparative analysis of hydrogen diffusion activation enthalpies between M1 and M2 configurations indicates that M1 is more stable than M2 at high temperatures, aligning with previous computational results (Panero, 2010).

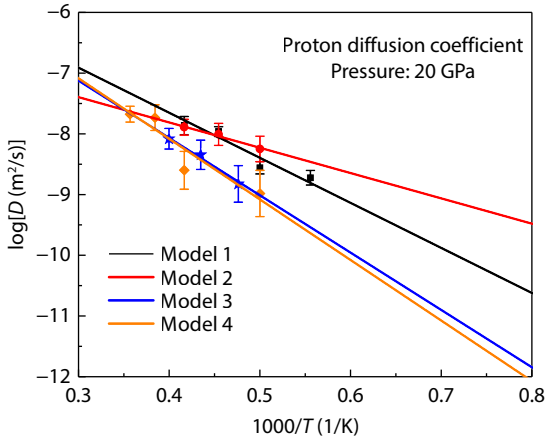

Figure 6. Calculated proton diffusion coefficient as a function of the reciprocal temperature for different models. The bulk diffusion coefficients of the M1–M5 configurations are denoted by black squares, red circles, blue stars, and orange diamonds, respectively. Error bars correspond to the standard uncertainty with fitting the MSD.

5.3 Implications of the Electrical Conductivity of the MTZ

Previous experiments have shown that, for dry ringwoodite, the conductivity of silicate minerals under mantle conditions is primarily governed by ionic conductivity and small polaron conduction. Ionic conduction is characterized by the movement of Mg^{2+} ions into interstitial sites, while electronic conduction involves small polaron conduction, including the transfer of electrons or holes between Fe^{2+} and Fe^{3+}. Moreover, at high temperatures, the conductivity of hydrous ringwoodite is mainly dominated by proton diffusion, contributing to proton conductivity (Sun W et al., 2015). We calculate the conductivity using the following equation:

$$\sigma_{\text{bulk}} = \sigma_{\text{dry}} + \sigma_{\text{water}}. \tag{7}$$

In this investigation, we determined the aggregate conductivity of dry ringwoodite, including the sum of ionic conductivity and hopping conductivity that are referenced from Yoshino et al. (2008). Combined Equations (1) and (7), we conducted a computational analysis to describe the temperature-dependent trends in proton and bulk conductivity for models with differing water content, as depicted in Figure 7. Evidently, the conductivity of hydrous ringwoodite is strongly contingent on its water content, with an increase of approximately 1–2 orders of magnitude observed at just about 1.0 wt% water content. It's pertinent to highlight that, for the M5 hydrated configuration, our AIMD simulations have a higher cutoff temperature relative to the M1–M4 configurations.

As a result, we have learned that different constitution water configurations can co-exist in a wider range of systems (Purevjav et al., 2014). Specially, Huang XG et al. (2005) conducted measurements solely on the bulk conductivity of hydrous ringwoodite. Therefore, we computed their proton conductivity by subtracting the dry ringwoodite from Yoshino et al. (2008). In Figure 8, we show the influence of water content and temperature on the conductivity within the MTZ region for hydrous ringwoodite, comparing results from previous high-temperature and high-pressure experiments with those of our study. The calculated bulk conductivity for models featuring high water content (exceeding 1.0 wt%) in this study exhibits lower deviation from the measurements by Huang XG et al. (2005), but presents substantial disparities relative to the results of Yoshino et al. (2008) and Zhang BH et al. (2019). In elucidating this conundrum, it is imperative to consider two pivotal points. Firstly, the experiments of Huang XG

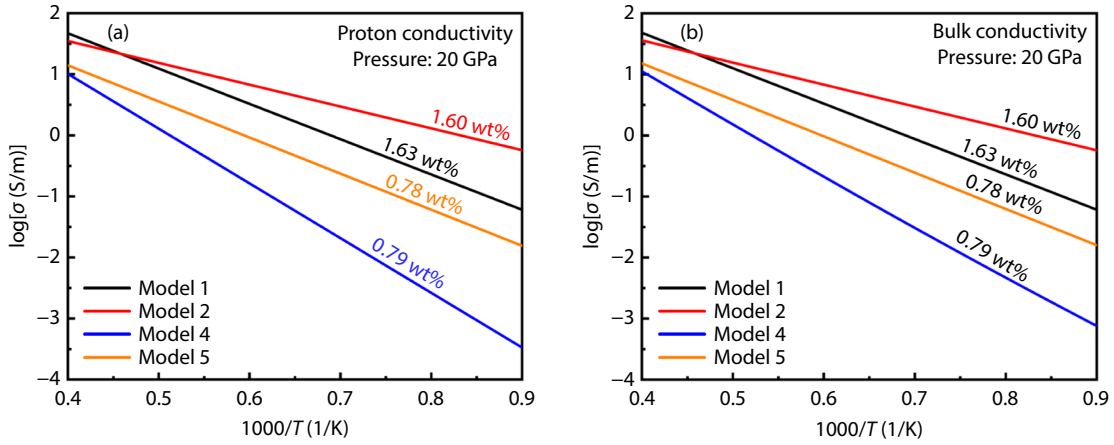

Figure 7. Calculated proton conductivity (a) and bulk conductivity (b) as a function of the reciprocal temperature for different models. Ion defect conduction and small polaron conduction were determined from the conductivity of dry ringwoodite.

et al. (2005) employed smaller sample sizes of ringwoodite (5–10 μm), introducing a significant two-order-of-magnitude reduction in electrical conductivity compared to the samples used by Yoshino et al. (2008) (100–500 μm). Secondly, from a microscopic perspective, protons in high-water-content models exhibit intense coupling with other charged defects through Coulomb forces, the force strength of which depends on the average ion distance. Consequently, both the small experimental sample sizes and the theoretically high-water-content models can significantly impact the results. As shown in Figure 8, the conductivity of the model with a water content of 1.19 wt% in this study is higher at high temperatures than that of the sample with a water content of 1.0 wt% in the experiment of Yoshino et al. (2008). This sheds light on previous analyses, suggesting the existence of a complex and strong interaction between the protons and the defects in the high-water-content model, as well as the potential effect of the high density of hydrogen on the mobility of the protons. It is worth mentioning that the results in the low-temperature section are subject to some degree of error as they are fitted from the results at high temperatures.

Moreover, in this investigation, a water content of 0.79 wt% effectively explains the observed conductivities in both the deeper MTZ in the Craton region and the shallower MTZ in the North Pacific region. The water content in this study also aligns with the ranges achieved in high-pressure experiments (Smyth et al., 2003). In addition, the experimentally derived conductivity results from previous comparisons of constructed water content models agree reasonably well with the average of globally averaged actual model-measured conductivity (Kelbert et al., 2009; Pearson et al., 2014).

6. Conclusions

In summary, our calculations for the constructed low-water-content model (0.79 wt%) show notable consistency with the observed conductivity in the stable Craton region of the MTZ. Importantly, these computations provide a useful reference for exploring the conductivity mechanism of water-bearing minerals, suggesting that constructing a larger model to reduce proton density and minimize Coulomb interactions would yield more accurate proton mobility. However, for the crystal lattice model of ringwoodite, constructing a large system for AIMD simulations while maintaining system symmetry is both challenging and computationally expensive. Consequently, we aim to explore the

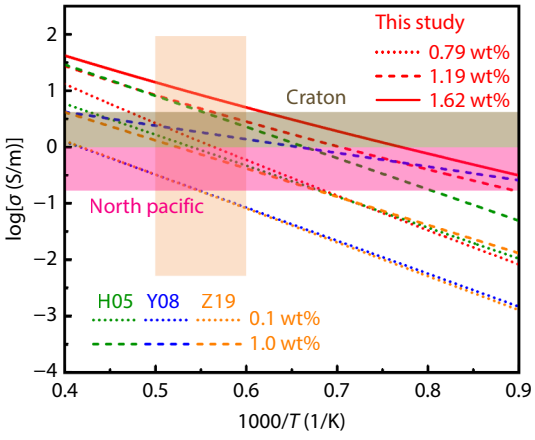

Figure 8. Plot of the conductivity of ringwoodite as a function of temperature and water content. The dark brown and pink areas (horizontal) represent the range of conductivity values observed in the stable cratons region (Schultz et al., 1993; Lizarralde et al., 1995; Neal et al., 2000; Jones, 2003; Evans et al., 2005; Kuvshinov et al., 2005; Seama et al., 2007; Yoshino et al., 2009) and in the MTZ below of the North Pacific region (Shimizu et al., 2010), respectively. H05, Y08, and Z19 represent the conductivity data with different water contents reported in the papers of Huang XG et al. (2005), Yoshino et al. (2008), and Zhang BH et al. (2019), respectively, which are denoted by green, blue and orange solid lines. The water contents in this study are arranged in descending order using red lines (0.79 wt%), dashed lines (1.19 wt%), and dotted lines (1.62 wt%). These values represent the arithmetic mean conductivity at different averaged water contents: 0.79 wt% (Models 4 & 5), 1.19 wt% (Models 1, 2, 4, & 5), and 1.62 wt% (Models 1 & 2). Previously calculated absolute temperatures at depths of 520–660 km (from about 1700 K to about 2000 K; Katsura et al., 2010) are also marked as light orange rectangular areas (vertical). The hydrous ringwoodite conductivity was corrected by ionic conductivity and hopping conductivity referred from dry ringwoodite reported by Yoshino et al. (2008).

integration of deep learning potentials with classical molecular dynamics methods in the future, specifically using Deep Potential Molecular Dynamics (DPMD), which strikes a balance between efficiency and accuracy.

Data Availability

The data underlying this paper will be shared on reasonable request to the corresponding author.

Declaration of Interest Statement

No conflict of interest exists in the submission of this manuscript, and the manuscript is approved by all authors for publication. I would like to declare on behalf of my co-authors that the work described was original research that has not been published previously, nor considered for publication elsewhere, in whole or in part.

Acknowledgment

This work is supported by the National Natural Science Foundation of China (41930112, 91755215), and the Sichuan Students' Innovation and entrepreneurship training program (s202310616086). All the *ab initio* simulations were performed at Chengdu Supercomputing Center.

References

Alexandrov, V., Neumann, A., Scherer, M. M., and Rosso, K. M. (2013). Electron exchange and conduction in nontronite from first-principles. *J. Phys. Chem. C*, *117*(5), 2032–2040. https://doi.org/10.1021/jp3110776

Baroni, S., De Gironcoli, S., Dal Corso, A., and Giannozzi, P. (2001). Phonons and related crystal properties from density-functional perturbation theory. *Rev. Mod. Phys.*, *73*(2), 515–562. https://doi.org/10.1103/RevModPhys.73.515

Blanchard, M., Ingrin, J., Balan, E., Kovács, I., and Withers, A. C. (2017). Effect of iron and trivalent cations on OH defects in olivine. *Am. Mineral.*, *102*(2), 302–311. https://doi.org/10.2138/am-2017-5777

Blöchl, P. E. (1994). Projector augmented-wave method. *Phys. Rev. B*, *50*(24), 17953–17979. https://doi.org/10.1103/PhysRevB.50.17953

Chakraborty, S. (2010). Diffusion coefficients in olivine, wadsleyite and ringwoodite. *Rev. Mineral. Geochem.*, *72*(1), 603–639. https://doi.org/10.2138/rmg.2010.72.13

Dai, L. D., and Karato, S. I. (2014). High and highly anisotropic electrical conductivity of the asthenosphere due to hydrogen diffusion in olivine. *Earth Planet. Sci. Lett.*, *408*, 79–86. https://doi.org/10.1016/j.epsl.2014.10.003

Du Frane, W. L., and Tyburczy, J. A. (2012). Deuterium-hydrogen exchange in olivine: Implications for point defects and electrical conductivity. *Geochem. Geophys. Geosyst.*, *13*(3), Q03004. https://doi.org/10.1029/2011GC003895

Evans, R. L., Hirth, G., Baba, K., Forsyth, D., Chave, A., and Mackie, R. (2005). Geophysical evidence from the MELT area for compositional controls on oceanic plates. *Nature*, *437*(7056), 249–252. https://doi.org/10.1038/nature04014

Evans, R. L., Wannamaker, P. E., McGary, R. S., and Elsenbeck, J. (2014). Electrical structure of the central Cascadia subduction zone: The EMSLAB Lincoln Line revisited. *Earth Planet. Sci. Lett.*, *402*, 265–274. https://doi.org/10.1016/j.epsl.2013.04.021

He, Y., Dai, L. D., Kim, D. Y., Li, H. P., and Karato, S. I. (2021a). Thermal ionization of hydrogen in hydrous olivine with enhanced and anisotropic conductivity. *J. Geophys. Res.: Solid Earth*, *126*(9), e2021JB022939. https://doi.org/10.1029/2021JB022939

He, Y., Sun, S. C., and Li, H. P. (2021b). *Ab initio* molecular dynamics investigation of the elastic properties of superionic Li_2O under high temperature and pressure. *Phys. Rev. B*, *103*(17), 174105. https://doi.org/10.1103/PhysRevB.103.174105

Huang, X. G., Xu, Y. S., and Karato, S. I. (2005). Water content in the transition zone from electrical conductivity of wadsleyite and ringwoodite. *Nature*, *434*(7034), 746–749. https://doi.org/10.1038/nature03426

Jones, A. (2003). The electrical structure of the Slave craton. *Lithos*, *71*(2-4), 505–527. https://doi.org/10.1016/j.lithos.2003.08.001

Karato, S. I. (1990). The role of hydrogen in the electrical conductivity of the upper mantle. *Nature*, *347*(6290), 272–273. https://doi.org/10.1038/347272a0

Karato, S. I. (2019). Some remarks on hydrogen-assisted electrical conductivity in olivine and other minerals. *Prog. Earth Planet. Sci.*, *6*, 55. https://doi.org/10.1186/s40645-019-0301-2

Katsura, T., Yoneda, A., Yamazaki, D., Yoshino, T., and Ito, E. (2010). Adiabatic temperature profile in the mantle. *Phys. Earth Planet. Inter.*, *183*(1-2), 212–218. https://doi.org/10.1016/j.pepi.2010.07.001

Kelbert, A., Schultz, A., and Egbert, G. (2009). Global electromagnetic induction constraints on transition-zone water content variations. *Nature*, *460*(7258), 1003–1006. https://doi.org/10.1038/nature08257

Kim, S., Wang, X. W., Jang, J., Eom, K., Clegg, S. L., Park, G. S., and Di Tommaso, D. (2020). Hydrogen-bond structure and low-frequency dynamics of electrolyte solutions: Hydration numbers from *ab initio* water reorientation dynamics and dielectric relaxation spectroscopy. *ChemPhysChem*, *21*(20), 2334–2346. https://doi.org/10.1002/cphc.202000498

Kohlstedt, D. L., Keppler, H., and Rubie, D. C. (1996). Solubility of water in the *α*, *β* and *γ* phases of $(Mg, Fe)_2SiO_4$. *Contrib. Mineral. Petrol.*, *123*(4), 345–357. https://doi.org/10.1007/s004100050161

Kohn, W., and Sham, L. J. (1965). Self-consistent equations including exchange and correlation effects. *Phys. Rev.*, *140*(4A), A1133–A1138. https://doi.org/10.1103/PhysRev.140.A1133

Krenzer, G., Kim, C. E., Tolborg, K., Morgan, B. J., and Walsh, A. (2022). Anharmonic lattice dynamics of superionic lithium nitride. *J. Mater. Chem. A*, *10*(5), 2295–2304. https://doi.org/10.1039/D1TA07631K

Kresse, G., and Furthmüller, J. (1996). Efficiency of *ab-initio* total energy calculations for metals and semiconductors using a plane-wave basis set. *Comput. Mater. Sci.*, *6*(1), 15–50. https://doi.org/10.1016/0927-0256(96)00008-0

Kudoh, Y., Kuribayashi, T., Mizobata, H., and Ohtani, E. (2000). Structure and cation disorder of hydrous ringwoodite, γ-$Mg_{1.89}Si_{0.98}H_{0.30}O_4$. *Phys. Chem. Miner.*, *27*(7), 474–479. https://doi.org/10.1007/s002690000091

Kühne, T. D., and Khaliullin, R. Z. (2014). Nature of the asymmetry in the hydrogen-bond networks of hexagonal ice and liquid water. *J. Am. Chem. Soc.*, *136*(9), 3395–3399. https://doi.org/10.1021/ja411161a

Kuvshinov, A., Utada, H., Avdeev, D., and Koyama, T. (2005). 3-D modelling and analysis of *Dst C*-responses in the North Pacific Ocean region, revisited. *Geophys. J. Int.*, *160*(2), 505–526. https://doi.org/10.1111/j.1365-246X.2005.02477.x

Li, L., Brodholt, J., and Alfè, D. (2009). Structure and elasticity of hydrous ringwoodite: A first principle investigation. *Phys. Earth Planet. Inter.*, *177*(3-4), 103–115. https://doi.org/10.1016/j.pepi.2009.07.007

Liu, C., Gao, H., Wang, Y., Needs, R. J., Pickard, C. J., Sun, J., Wang, H. T., and Xing, D. Y. (2019). Multiple superionic states in helium–water compounds. *Nat. Phys.*, *15*(10), 1065–1070. https://doi.org/10.1038/s41567-019-0568-7

Lizarralde, D., Chave, A., Hirth, G., and Schultz, A. (1995). Northeastern Pacific mantle conductivity profile from long-period magnetotelluric sounding using Hawaii-to-California submarine cable data. *J. Geophys. Res.: Solid Earth*, *100*(B9), 17837–17854. https://doi.org/10.1029/95JB01244

Marzotto, E., Hsieh, W. P., Ishii, T., Chao, K. H., Golabek, G. J., Thielmann, M., and Ohtani, E. (2020). Effect of water on lattice thermal conductivity of ringwoodite and its implications for the thermal evolution of descending slabs. *Geophys. Res. Lett.*, *47*(13), e2020GL087607. https://doi.org/10.1029/2020GL087607

McGary, R. S., Evans, R. L., Wannamaker, P. E., Elsenbeck, J., and Rondenay, S. (2014). Pathway from subducting slab to surface for melt and fluids beneath Mount Rainier. *Nature*, *511*(7509), 338–340. https://doi.org/10.1038/nature13493

Neal, S. L., Mackie, R. L., Larsen, J. C., and Schultz, A. (2000). Variations in the electrical conductivity of the upper mantle beneath North America and the

Pacific Ocean. *J. Geophys. Res.: Solid Earth*, *105*(B4), 8229–8242. https://doi.org/10.1029/1999JB900447

Panero, W. R. (2010). First principles determination of the structure and elasticity of hydrous ringwoodite. *J. Geophys. Res.: Solid Earth*, *115*(B3), B03203. https://doi.org/10.1029/2008JB006282

Pearson, D. G., Brenker, F. E., Nestola, F., McNeill, J., Nasdala, L., Hutchison, M. T., Matveev, S., Mather, K., Silversmit, G., … Vincze, L. (2014). Hydrous mantle transition zone indicated by ringwoodite included within diamond. *Nature*, *507*(7491), 221–224. https://doi.org/10.1038/nature13080

Perdew, J. P., Burke, K., and Ernzerhof, M. (1996). Generalized gradient approximation made simple. *Phys. Rev. Lett.*, *77*(18), 3865–3868. https://doi.org/10.1103/PhysRevLett.77.3865

Purevjav, N., Okuchi, T., Tomioka, N., Abe, J., and Harjo, S. (2014). Hydrogen site analysis of hydrous ringwoodite in mantle transition zone by pulsed neutron diffraction. *Geophys. Res. Lett.*, *41*(19), 6718–6724. https://doi.org/10.1002/2014GL061448

Roberts, J. J., and Tyburczy, J. A. (1999). Partial-melt electrical conductivity: Influence of melt composition. *J. Geophys. Res.: Solid Earth*, *104*(B4), 7055–7065. https://doi.org/10.1029/1998JB900111

Ross, N. L., Gibbs, G. V., and Rosso, K. M. (2003). Potential docking sites and positions of hydrogen in high-pressure silicates. *Am. Mineral.*, *88*(10), 1452–1459. https://doi.org/10.2138/am-2003-1009

Rossman, G. R. (1996). Studies of OH in nominally anhydrous minerals. *Phys. Chem. Miner.*, *23*(4-5), 299–304. https://doi.org/10.1007/BF00207777

Schultz, A., Kurtz, R. D., Chave, A. D., and Jones, A. G. (1993). Conductivity discontinuities in the upper mantle beneath a stable craton. *Geophys. Res. Lett.*, *20*(24), 2941–2944. https://doi.org/10.1029/93GL02833

Seama, N., Baba, K., Utada, H., Toh, H., Tada, N., Ichiki, M., and Matsuno, T. (2007). 1-D electrical conductivity structure beneath the Philippine Sea: Results from an ocean bottom magnetotelluric survey. *Phys. Earth Planet. Inter.*, *162*(1-2), 2–12. https://doi.org/10.1016/j.pepi.2007.02.014

Shimizu, H., Koyama, T., Baba, K., and Utada, H. (2010). Revised 1-D mantle electrical conductivity structure beneath the north Pacific. *Geophys. J. Int.*, *180*(3), 1030–1048. https://doi.org/10.1111/j.1365-246X.2009.04466.x

Shimojuku, A., Kubo, T., Ohtani, E., Nakamura, T., Okazaki, R., Dohmen, R., and Chakraborty, S. (2009). Si and O diffusion in (Mg, Fe)$_2$SiO$_4$ wadsleyite and ringwoodite and its implications for the rheology of the mantle transition zone. *Earth Planet. Sci. Lett.*, *284*(1-2), 103–112. https://doi.org/10.1016/j.epsl.2009.04.014

Smyth, J. R., Holl, C. M., Frost, D. J., Jacobsen, S. D., Langenhorst, F., and Mccammon, C. A. (2003). Structural systematics of hydrous ringwoodite and water in Earth's interior. *Am. Mineral.*, *88*(10), 1402–1407. https://doi.org/10.2138/am-2003-1001

Sun, W., Yoshino, T., Sakamoto, N., and Yurimoto, H. (2015). Hydrogen self-diffusivity in single crystal ringwoodite: Implications for water content and distribution in the mantle transition zone. *Geophys. Res. Lett.*, *42*(16), 6582–6589. https://doi.org/10.1002/2015GL064486

Togo, A., Chaput, L., Tadano, T., and Tanaka, I. (2023). Implementation strategies in phonopy and phono3py. *J. Phys.: Condens. Matter*, *35*, 353001. https://doi.org/10.1088/1361-648X/acd831

Umemoto, K., Wentzcovitch, R. M., Hirschmann, M. M., Kohlstedt, D. L., and Withers, A. C. (2011). First-principles investigation of hydrous defects and IR frequencies in forsterite: The case for Si vacancies. *Am. Mineral.*, *96*(10), 1475–1479. https://doi.org/10.2138/am.2011.3720

Verma, A. K., and Karki, B. B. (2009). *Ab initio* investigations of native and protonic point defects in Mg$_2$SiO$_4$ polymorphs under high pressure. *Earth Planet. Sci. Lett.*, *285*(1-2), 140–149. https://doi.org/10.1016/j.epsl.2009.06.009

Walker, A. M., Hermann, J., Berry, A. J., and O'Neill, H. S. C. (2007). Three water sites in upper mantle olivine and the role of titanium in the water weakening mechanism. *J. Geophys. Res.: Solid Earth*, *112*(B5), B05211. https://doi.org/10.1029/2006JB004620

Wang, W. Z., Zhang, H., Brodholt, J. P., and Wu, Z. Q. (2021). Elasticity of hydrous ringwoodite at mantle conditions: Implication for water distribution in the lowermost mantle transition zone. *Earth Planet. Sci. Lett.*, *554*, 116626. https://doi.org/10.1016/j.epsl.2020.116626

Wang, W. Z., and Wu, Z. Q. (2022). A first-principles study of water in wadsleyite and ringwoodite: Implication for the 520 km discontinuity. *Am. Mineral.*, *107*(7), 1361–1368. https://doi.org/10.2138/am-2021-7929

Wannamaker, P. E., Caldwell, T. G., Jiracek, G. R., Maris, V., Hill, G. J., Ogawa, Y., Bibby, H. M., Bennie, S. L., and Heise, W. (2009). Fluid and deformation regime of an advancing subduction system at Marlborough, New Zealand. *Nature*, *460*(7256), 733–736. https://doi.org/10.1038/nature08204

Withers, A. C., Hirschmann, M. M., and Tenner, T. J. (2011). The effect of Fe on olivine H_2O storage capacity: Consequences for H_2O in the martian mantle. *Am. Mineral.*, *96*(7), 1039–1053. https://doi.org/10.2138/am.2011.3669

Worzewski, T., Jegen, M., Kopp, H., Brasse, H., and Taylor Castillo, W. (2011). Magnetotelluric image of the fluid cycle in the Costa Rican subduction zone. *Nat. Geosci.*, *4*(2), 108–111. https://doi.org/10.1038/ngeo1041

Yang, X. Z., Keppler, H., McCammon, C., Ni, H. W., Xia, Q. K., and Fan, Q. C. (2011). Effect of water on the electrical conductivity of lower crustal clinopyroxene. *J. Geophys. Res.: Solid Earth*, *116*(B4), B04208. https://doi.org/10.1029/2010JB008010

Ye, Y., Brown, D. A., Smyth, J. R., Panero, W. R., Jacobsen, S. D., Chang, Y. Y., Townsend, J. P., Thomas, S, M., Hauri, E. H., … Frost, D. J. (2012). Compressibility and thermal expansion of hydrous ringwoodite with 2.5 (3) wt% H_2O. *Am. Mineral.*, *97*(4), 573–582. https://doi.org/10.2138/am.2012.4010

Yoshino, T., Manthilake, G., Matsuzaki, T., and Katsura, T. (2008). Dry mantle transition zone inferred from the conductivity of wadsleyite and ringwoodite. *Nature*, *451*(7176), 326–329. https://doi.org/10.1038/nature06427

Yoshino, T., Matsuzaki, T., Shatskiy, A., and Katsura, T. (2009). The effect of water on the electrical conductivity of olivine aggregates and its implications for the electrical structure of the upper mantle. *Earth Planet. Sci. Lett.*, *288*(1-2), 291–300. https://doi.org/10.1016/j.epsl.2009.09.032

Yu, Y. G., and Wentzcovitch, R. M. (2006). Density functional study of vibrational and thermodynamic properties of ringwoodite. *J. Geophys. Res.: Solid Earth*, *111*(B12), B12202. https://doi.org/10.1029/2006JB004282

Zhang, B. H., Yoshino, T., and Zhao, C. C. (2019). The effect of water on Fe-Mg interdiffusion rates in ringwoodite and implications for the electrical conductivity in the mantle transition zone. *J. Geophys. Res.: Solid Earth*, *124*(3), 2510–2524. https://doi.org/10.1029/2018JB016415

Zhao, Y. H., Ginsberg, S. B., and Kohlstedt, D. L. (2004). Solubility of hydrogen in olivine: dependence on temperature and iron content. *Contrib. Mineral. Petrol.*, *147*(2), 155–161. https://doi.org/10.1007/s00410-003-0524-4